RASĀYAN *J. Chem.*
Vol. 19 | No. 4 | 2438-2449 | October-December | 2026
ISSN: 0974-1496 | e-ISSN: 0976-0083 | CODEN: RJCABP
http://www.rasayanjournal.com
http://www.rasayanjournal.co.in

DOPANT ENGINEERING OF CERIUM OXIDE THIN FILMS VIA ULTRA SPRAY PYROLYSIS: COMPARATIVE EVALUATION OF Fe, Ni, Cu, AND Zr DOPING FOR SUPERIOR ANTIMICROBIAL COATINGS

S. S. Salunkhe[1,2], S. R. Gadale[1], S. S. Shukla[1], and A. B. Pawar[1,✉]
[1]Bharati Vidyapeeth (Deemed to be University), Yashwantrao Mohite College of Arts, Science and Commerce, Pune-38, Maharashtra
[2]Dr. Patangrao Kadam Mahavidyalaya, Ramanandnagar (Burli), (MH), India
✉Corresponding author: abpawar@yahoo.com

ABSTRACT
The current research describes the preparation of cerium oxide (CeO_2) thin films doped with iron, nickel, copper, and zirconium through the ultrasonic spray pyrolysis method, followed by an investigation of the structural, morphological, and antibacterial behaviour of the synthesised thin films. XRD analysis revealed that all prepared thin films have a cubic fluorite structure of CeO_2, with a difference in crystallite size due to the doping effect and broadening of diffraction peaks. Field emission scanning electron microscopy (FE-SEM) showed a nano-structured, porous and uniformly distributed grain structure for all the doped thin films. EDX spectroscopy confirmed the successful doping of CeO_2 with the dopants, with high purity of elements. The antibacterial activity of the doped thin films was studied against four strains of bacteria, viz., Escherichia coli, Pseudomonas aeruginosa, Staphylococcus aureus and Bacillus subtilis, by the agar well diffusion assay method. Out of the four dopants, Fe and Zr were found to be more effective as compared to Cu and Ni. These results confirm that dopant engineering offers an effective approach to modulate the characteristics of the surface and structure of ceria thin films, thus representing a substantial step forward in the development of high-quality antimicrobial coatings. This research work is closely linked to the Sustainable Development Goal-3 (Good Health and Well-being) as advanced nanostructured materials were created to combat pathogen-related bacterial infections.
Keywords: Cerium Oxide Thin Films, Doping, Ultra-Spray Pyrolysis, XRD, FE-SEM, EDX, Antibacterial Activity.
RASĀYAN *J. Chem.*, Vol. 19, No.4, 2026

INTRODUCTION

Cerium dioxide (CeO_2) is a rare-earth functional oxide that has attracted significant interest because of its impressive physicochemical properties. It has a high oxygen storage capacity, great thermal stability, and the ability to switch between Ce^{3+} and Ce^{4+} states. These qualities make CeO_2 a good fit for several applications, such as catalysis, solid oxide fuel cells, gas sensors, and biomedical materials. CeO_2 has more active sites and improved surface reactivity in its nanoscale form, which expands its potential applications. Metal ion doping is a useful method to further adjust CeO_2's characteristics for specific uses. The addition of isovalent or aliovalent metal ions to the ceria lattice modifies surface charge, introduces oxygen vacancies, changes the crystal structure, and affects grain boundary behavior.[3] Both physicochemical and biological performance may be greatly impacted by these modifications. Specifically, doped ceria nanomaterials have demonstrated improved antibacterial activity because of increased defect-induced reactivity, better surface interactions with microbial membranes, and increased production of reactive oxygen species (ROS). Fe, Ni, Cu, and Zr were selected as dopants for this study because of their special capacity to affect the structural and functional properties of CeO_2. Each of these dopants offers unique benefits that may increase the material's biological and structural functionality.[5-6] Iron (Fe) is known to improve redox behaviour and electron transfer, Nickel (Ni) introduces high lattice strain and defect density, Copper (Cu) is highly regarded for its intrinsic antimicrobial properties and catalytic synergy with ceria, and Zirconium (Zr) contributes to lattice stabilisation and improved crystallinity due to its ionic radius being close to that of Ce^{+}. Ultrasonic spray pyrolysis (USP) is used as a synthesis method to create these nanostructured thin films. The uniform deposition of doped nanoparticles

http://doi.org/10.31788/RJC.2026.1949786
This work is licensed under a CC BY 4.0 license.

onto substrates is made possible by USP, a scalable, continuous, and economical technique. Precursor solutions are atomised into tiny droplets and then thermally broken down to produce uniformly doped thin films with regulated composition and morphology.[7-10] The current study's goal is to create CeO_2 thin films doped with Fe, Ni, Cu, and Zr separately using the ultra-spray pyrolysis method and thoroughly assess their morphological, structural, and antimicrobial characteristics. The films are evaluated using sophisticated characterisation techniques like energy-dispersive X-ray spectroscopy (EDX), field-emission scanning electron microscopy (FE-SEM), and X-ray diffraction (XRD). Additionally, their potential in antimicrobial applications is investigated by testing their antibacterial efficacy against specific human pathogens. Additionally, this research is in line with SDG-3 (Good Health and Well-Being), which focuses on reducing infectious diseases by designing advanced material-based antimicrobial surfaces.

Materials and Methods

Doped ceria thin films were prepared using the ultra-spray pyrolysis (USP) method. During this process, the precursor solution is turned into an aerosol and transferred onto a heated substrate for thermal decomposition and thin film growth. Before deposition, the glass slides were cleaned properly with distilled water, acetone, and ethanol, followed by drying of the slides at ambient temperature. For each transition-metal dopant, a corresponding 50 mL aqueous precursor solution was prepared. Cerium(III) nitrate hexahydrate served as the main precursor material, while $FeCl_3 \cdot 6H_2O$, $Ni(NO_3)_2 \cdot 6H_2O$, $Cu(NO_3)_2 \cdot 3H_2O$, and $ZrOCl_2 \cdot xH_2O$ were used to provide the dopants of Fe, Ni, Cu, and Zr, respectively. All metal ion concentrations in the precursors were kept constant at 0.02 M. Each precursor solution was supplied to the USP system at a flow rate of 50 mL h^{-1}. Subsequently, the aerosols generated were transferred to a furnace operated at 350 °C for thermal decomposition of the solutions. The synthesis was repeated for each dopant as well as for undoped ceria for comparison. The structural and compositional properties of the thin films were characterised using X-ray diffraction (XRD), field emission scanning electron microscopy (FE-SEM), and energy-dispersive X-ray spectroscopy (EDX). XRD analysis was conducted using a diffractometer equipped with Cu Kα radiation (λ = 1.5406 Å) to confirm the crystalline phases and calculate crystallite sizes using the Debye–Scherrer equation. The surface morphology was examined via FE-SEM, and elemental composition was analysed using EDX, which also provided elemental mapping to assess dopant distribution. The synthesised films were tested for their antimicrobial activity by the agar well diffusion method against Escherichia coli, Pseudomonas aeruginosa and Staphylococcus aureus. Nutrient agar plates were prepared and inoculated with standardised bacterial suspensions (0.5 McFarland standard), and wells were created in the agar to add 50 µL of each doped ceria suspension (10 mg/mL in DMSO). Streptomycin was used as a positive control and DMSO as a negative control. The plates were incubated at 37 °C for 24-48 h, and the inhibition zones were measured in mm. All antimicrobial tests were performed in triplicate to obtain reproducible and statistically valid results.

RESULTS AND DISCUSSION

XRD Analysis

The phase composition, crystallinity and structural changes upon doping of cerium oxide nanoparticles with transition metals (Cu, Ni) and a group IVB element (Zr) was determined by X-ray diffraction (XRD) analysis.[11] XRD patterns of the 0.02 M Cu, Ni, and Zr-doped samples in 0.025 M Ce precursor solutions showed characteristic diffraction peaks corresponding to the cubic fluorite structure of CeO_2 (JCPDS Card No. 34-0394),[12-13] confirming the successful synthesis without major impurity phases, as shown in Fig.-1 to 3.

Crystallinity and Peak Shifts

All the diffractograms show well-defined peaks at around 2θ = 28.5°, 47.4°, and 56.3° corresponding to (111), (220), and (311) crystallographic planes of CeO_2, respectively. These peaks were used for the crystallite size calculation by the Debye–Scherrer equation.[14] The width and intensity of peaks were different from sample to sample, which proved the influence of different dopants on the crystal structure:

Zr-Doped CeO_2: Shows the highest-intensity peaks and the sharpest peaks, which show that it is highly crystalline with large crystallite size. Zr^{4+} ions have an ionic radius of 0.84 Å, which is similar to that of

Ce^{4+} ions (0.97 Å). Cu Doped CeO_2: Moderately broad peaks have been noted, which indicate smaller crystal size and some strain in the lattice owing to the substitution of Cu^{2+}(0.73 Å). No specific peaks of CuO or Cu_2O have been noted, which indicates that Cu is uniformly doped. Ni-Doped CeO_2: Possessed the most diffuse peaks and the least intensity compared to other samples, hence having the smallest crystallite size, increased lattice strain, and high defect concentration. This is due to the replacement of Ce^{4+} with small-sized Ni^{2+} ions (0.69 Å).

Crystallite Size Estimation

Using the Debye–Scherrer formula:

$$D = K\lambda / \beta\cos\theta$$

Where:

D: Crystallite size (nm); K: Shape factor (0.9); λ: X-ray wavelength (1.5406 Å); β: FWHM in radians; θ: Bragg angle (in radians)

The average crystallite sizes were calculated from the most intense (111) peaks for each sample (centred at ~28.5°). The values are summarised in Table-1.

Figure-1 confirmed the Formation of a Fluorite-Type Cubic Structure with Slight Peak Shifts, Indicating Successful Incorporation of Zr, Cu, Ni and Fe ions into the CeO_2 Lattice without Secondary Phase Formation.

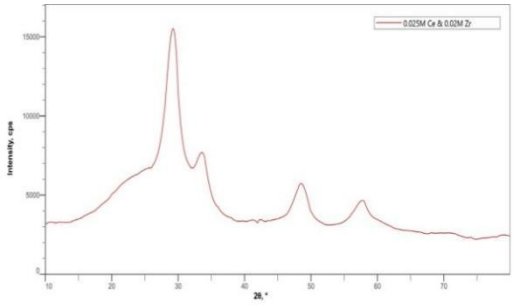

[A]

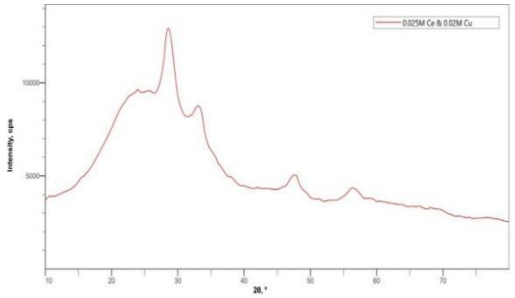

[B]

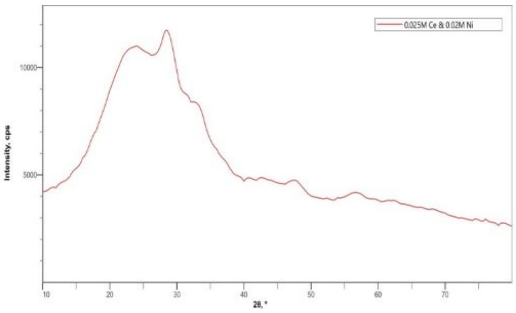

[C]

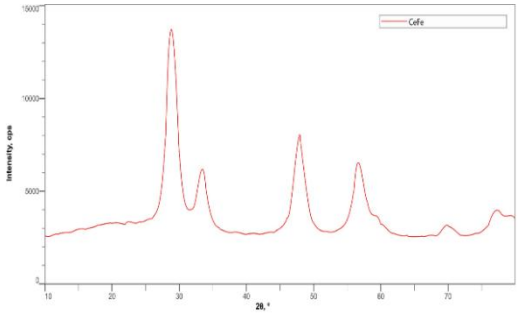

[D]

Fig.-1: XRD Patterns of [A] $Ce_{0.98}Zr_{0.02}O_2$, [B], $Ce_{0.98}Cu_{0.02}O_2$, [C] $Ce_{0.98}Ni_{0.02}O_2$ and [D] $Ce_{0.98}Fe_{0.02}O_2$

Table-1: Structural Properties of Doped Cerium Oxide Thin Films Determined by XRD Analysis

Sample	Main Peak (2θ)	FWHM (°)	Crystallite Size (nm)	Observations
Ce–Zr (0.02 M)	28.55	~0.20	~41.5	High crystallinity, minimal distortion
Ce–Cu (0.02 M)	28.53	~0.30	~27.6	Moderate peak broadening, defect formation
Ce–Ni (0.02 M)	28.51	~0.38	~21.8	Significant broadening, high lattice strain
Ce–Fe (0.02 M)	28.51	~0.34	~23.5	Shifting of the main peak and no secondary iron oxide peaks detected at low-to-moderate doping levels

The substitution of Ce^+ with smaller dopant cations introduced lattice strain, peak broadening, and a reduction in crystallite size. Zr^+ doping retained the integrity of the fluorite lattice, whereas Ni^{2+} and Cu^{2+}caused more structural distortion. These variations in structure can influence functional properties such as oxygen vacancy formation, redox behaviour, and catalytic/antimicrobial efficiency. X-ray diffraction (XRD) of iron-doped ceria (CeO_2) nanoparticles (Fig.-1D) confirms a single-phase, face-centred cubic fluorite structure matching standard ceria patterns (JCPDS 34-0394), with no secondary iron oxide peaks detected at low-to-moderate doping levels.

All primary peaks of ceria remain intact, showing that iron incorporation does not disrupt the fundamental CeO_2 lattice framework. The complete absence of separate Fe_2O_3 or FeO peaks indicates successful formation of a solid solution where Fe ions integrate into the ceria matrix ($Fe_xCe_{(1-x)}O_2$).

FE-SEM of Cu/CeO_2 Doped Thin Films

Figure-2, FE-SEM analysis of CuO/CeO_2 doped thin films reveals a regularly distributed and densely packed surface covered by nanostructures in the form of spherical to semispherical particles. Some particle aggregation occurred as a result of high surface energy, however no major agglomeration.[15] Most of the grain sizes were found in the nanoscale range, implying a well-developed nanostructure. The smooth texture as well as consistency of grains indicates minor disruption in structure if Cu is doped in the CeO_2 matrix; instead, the doped system is responsible for grain refinement.

The porous character of the films provides a high surface-to-volume ratio, thus enabling the material to be useful for catalysis, sensors and antimicrobial coatings; these are a few of its applications. In some areas, slight agglomeration may be linked to high-temperature reaction or sintering. Cu dopant seems to change the formation (nucleation) of CeO_2 nanocrystals, which is why the result is a compact, homogeneous, and crystalline microstructure with enhanced crystallinity and surface properties, which are advantageous for many functional applications.

FE-SEM of Fe/CeO_2 Doped Thin Films

Figure-3 FE-SEM images of FeO_2/CeO_2 doped thin films reveal a homogeneous and nanostructured surface with densely packed grains exhibiting mostly spherical to irregular shapes.[16] The nanoscale morphology suggests effective doping of Fe into the CeO_2 lattice, influencing the nucleation and resulting in uniform crystallite growth.

Minimal agglomeration and consistent grain distribution across the surface point toward controlled synthesis and good film quality. The presence of micro-porosity enhances the surface area, which is beneficial for applications in photocatalysis, gas sensing, and electrochemical systems. The refined and compact microstructure observed in the doped films indicates that Fe incorporation improves the morphological properties, thereby supporting their potential use in various functional nanomaterial-based applications.[17-18]

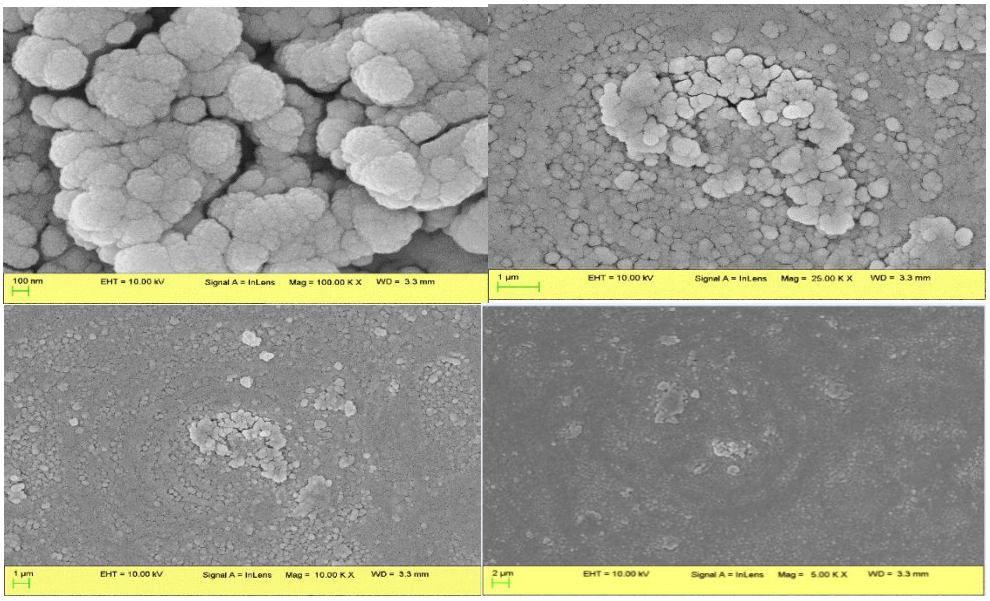

Fig.-2: FE-SEM images of Cu-Doped Cerium Oxide Reveal a Uniform Sand-Like Morphology at 1 µm Magnification, while at 100KX Magnification, the Nanoparticles Exhibit a Cauliflower Bud-Like Structure

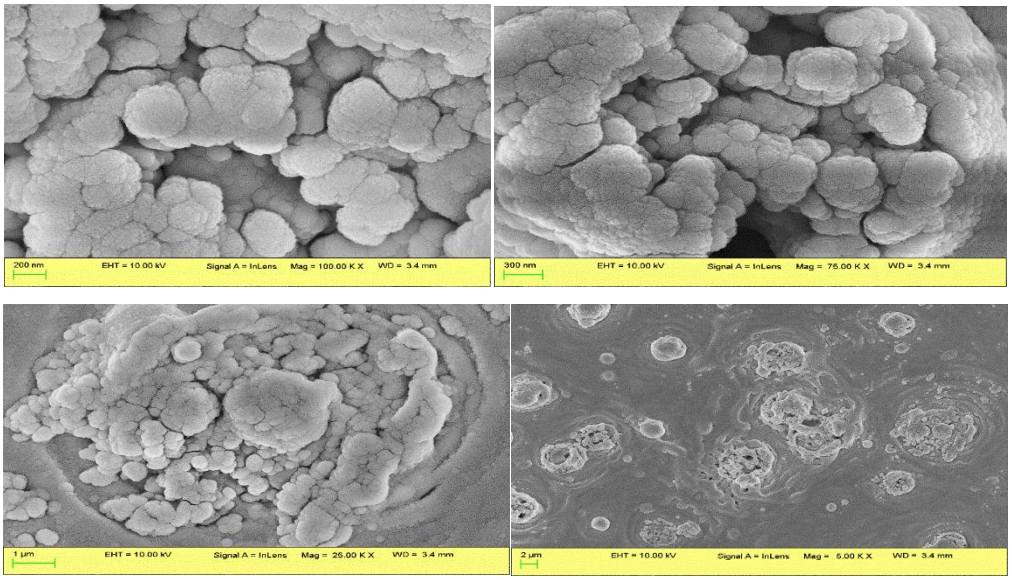

Fig.-3: FE-SEM Images of Fe-Doped Cerium Oxide Exhibit Spherical Particles Arranged in Cauliflower-Like Buds with a Porous Structure, Uniformly Distributed Across the Surface

FE-SEM of Ni/CeO_2 Doped Thin Films

The FE-SEM micrographs of NiO_2/CeO_2 doped thin films shown in Fig.-4 demonstrate a nanostructured surface morphology characterized by uniformly distributed and compactly arranged grains with predominantly spherical features.[19] The nanoscale particle size and smooth surface texture indicate successful synthesis of the thin films with minimal agglomeration. The presence of Ni in the CeO_2 matrix appears to influence the crystallite growth, leading to a refined and denser microstructure. Slight porosity

observed across the surface may enhance the active surface area, making the films suitable for catalytic, sensing, or energy storage applications.

Generally, the even structure, regulated particle size, and good surface features indicate a successful incorporation of Ni in the CeO_2 crystal lattice, ultimately leading to a more perfect microstructure that is useful for different nanotechnological applications.

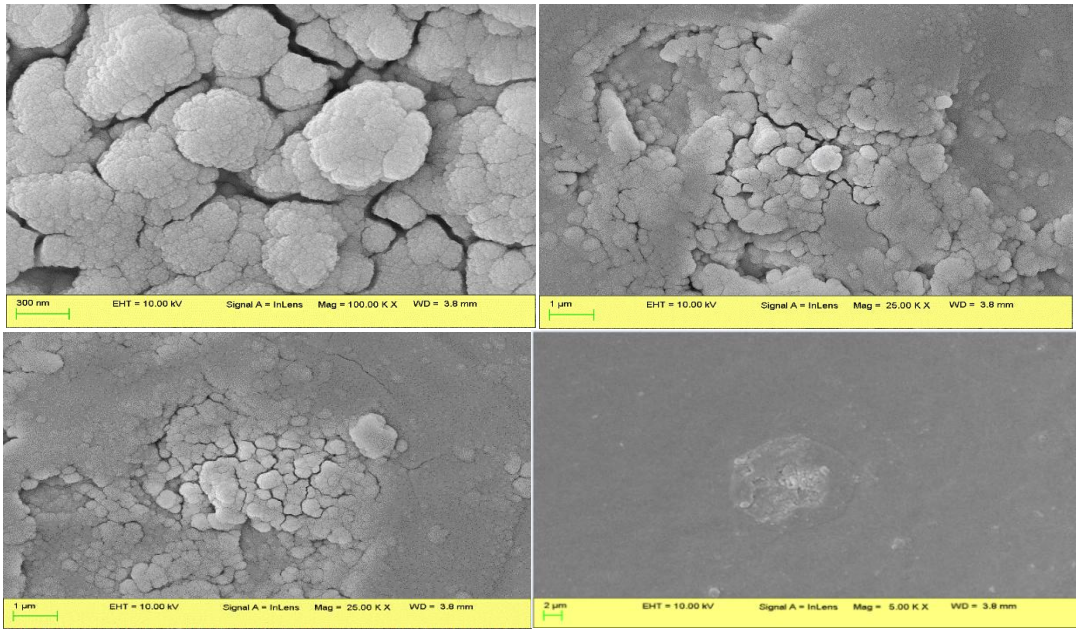

Fig.-4: Ni-doped CeO_2 Thin Films FE-SEM Images Show Distorted Spherical Particles that Have Very Low Agglomeration. Further magnification reveals that the nanoparticle patches look like they are Arranged in a Cauliflower Shape

FE-SEM of Zr/CeO_2 Doped Thin Film

Figure-5 FE-SEM images of zirconia and ceria thin films show nanostructured films with uniform distribution of grains with a relatively compact and spherical grain morphology (Fig.-5). Grain sizes are in the nanoparticle range, which means that the Zr is successfully introduced into the CeO_2 matrix, resulting in both crystallite size reduction and the surface homogeneity. The films have almost no agglomerates, and the porosity could improve the surface reactivity very efficiently, so the films would be a good starting point of materials for the above mentioned applications. The introduction of Zr increases the structure compactness and uniformity, resulting in enhanced microstructural features that are beneficial for the development of high-performance functional materials.

EDX Spectrum of Zr/CeO_2

From the EDX spectrum of Zr/CeO_2, the presence of zirconium (Zr), cerium (Ce), and oxygen (O) elements was established, which points to the fact that Zr has properly mixed with the CeO_2 matrix. The high level of Zr detected together with Ce proves the generation of a Zr-doped CeO_2 composite. The complete lack of impurities in the EDX spectrum not only confirms the purity of the created nanocomposite but also supports the validity of a stoichiometric substitution or doping mechanism of Zr in the CeO_2 lattice.[22-23]

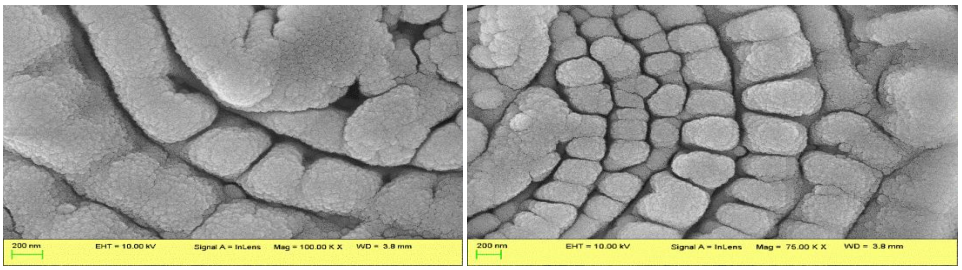

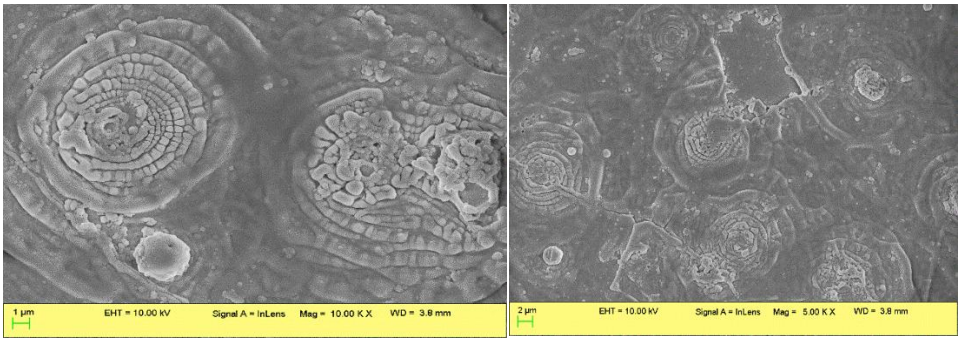

Fig.-5: FE-SEM Image of Zr-doped Cerium Oxide Shows Spherical Particles Forming a Bunch-Like Structure with 5–8 Interconnected Shells Arranged in a Circular Pattern, Exhibiting Homogeneous Particle Distribution

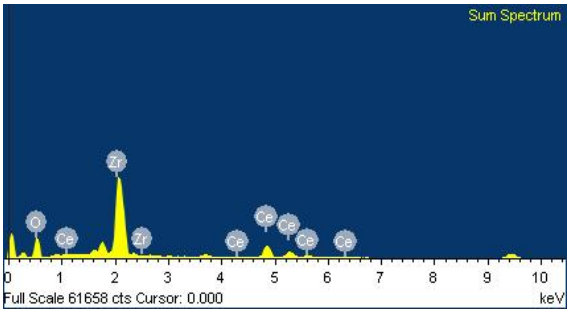

Fig.-6: EDX Spectrum of Zr/CeO_2 Confirms the Presence of Ce, O, and Zr, Indicating Successful Doping and Elemental Purity of the Thin Film

EDX Spectrum of Cu/CeO_2

The EDX analysis of Cu/CeO_2 shows fairly obvious peaks for copper (Cu), cerium (Ce), and oxygen (O), so it sort of confirms that Cu-doped CeO_2 nanocomposites were made. When you look at the Cu signals, they appear in the expected range, which checks its presence and also hints at a rather even dispersion inside the host matrix.[24] Overall, the results point to a successful synthesis of the composite, and they imply a pronounced interrelation between Cu and the CeO_2 framework; that interplay may affect its catalytic behaviour or even antimicrobial efficiency.

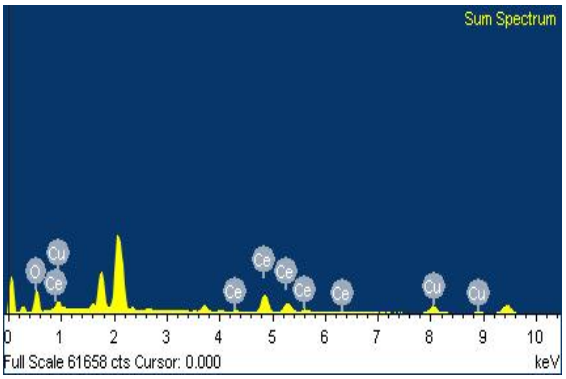

Fig.-7: EDX Spectrum of Cu/CeO_2 shows distinct peaks of Cu, Ce, and O, Confirming Successful Cu Doping and Uniform Distribution within the CeO_2 Matrix

EDX Spectrum of Ni/CeO_2

The EDX spectrum of Ni/CeO_2 shows the usual peaks for nickel (Ni), cerium (Ce), and oxygen (O), kinda pointing to the fact that Ni is really in, or at least was incorporated into, the CeO_2 framework. You can also see that peaks from foreign elements are basically absent, which backs up the chemical purity of the sample. Overall, these results support the doping plan that was aimed for, and they suggest that Ni has been properly embedded in the CeO_2 matrix, and that might help boost functional behaviour, for instance, redox activity, or maybe better electrical conductivity.[25]

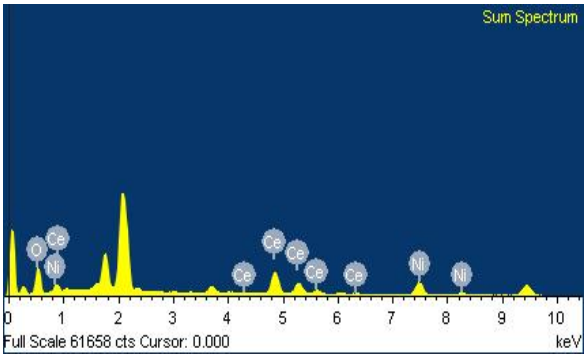

Fig.-8: EDX Spectrum of Ni/CeO_2 Shows Clear Peaks for Ni, Ce, and O, Confirming Successful Ni Doping and Chemical Purity of the Sample

EDX Spectrum of Fe/CeO_2

The EDX output for Fe/CeO_2 shows clear peaks from iron (Fe), cerium (Ce), and oxygen (O). This basically suggests that Fe has been incorporated into the CeO_2 framework successfully. In addition, the compositional profile shows a pretty even spread of the elements, so it supports that the Fe-doped CeO_2 is really formed, with not much other junk or contamination.[26] So overall, this points to the synthesis working as expected, and it also gives evidence that the CeO_2 structure got modified via iron doping, which in turn may alter its catalytic performance as well as its electronic character.

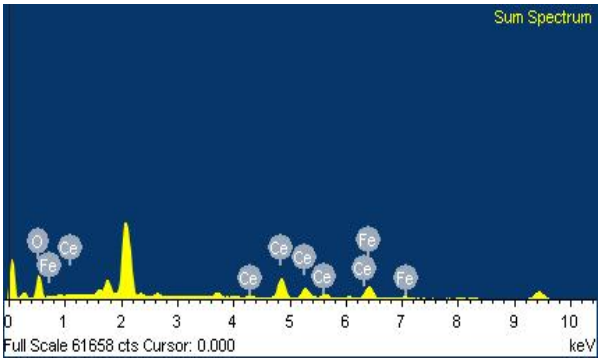

Fig.-9: EDX Spectrum of Fe/CeO_2 Shows Distinct Peaks for Fe, Ce, and O, Confirming Successful Fe Doping and Uniform Elemental Distribution Without Contamination

Antibacterial Activity

The antibacterial activity of various doped ceria nanoparticle samples was evaluated against four bacterial strains shown in Table-2, using the agar well diffusion method, and the zone of inhibition was measured in millimetres (mm).[27-28] Conc. of Stock Sol^n. 10 mg/mL; volume per well is 50 µl; quantity per well is 1.0 mg. Against *Escherichia coli*, Fe + Ce showed the highest inhibition zone of 17 ± 0.01 mm, followed by Zr + Ce (14 ± 0.02 mm) and Cu + Ce (09 ± 0.02 mm), while Ni + Ce exhibited no activity shown in fig 10. The standard streptomycin showed in Table-2, 26 ± 0.01 mm, and the control (DMSO) had no inhibition. Against *Pseudomonas aeruginosa*, Zr + Ce showed the highest antibacterial activity with a zone of 23 ± 0.01 mm, followed by Cu + Ce (17 ± 0.03 mm), Fe + Ce (16 ± 0.02 mm), and Ni + Ce (13 ± 0.01 mm). The standard antibiotic showed 25 ± 0.02 mm, while the control had no activity. The antibacterial activity of doped cerium oxide thin films against *Bacillus subtilis*: none of the doped ceria samples exhibited any antibacterial activity shown in Fig.-12. Only the standard streptomycin showed an inhibition zone of 19 ± 0.01 mm, and the control (DMSO) showed no inhibition. Table-2 also shows activity against *Staphylococcus aureus*; Fe + Ce demonstrated the highest zone of inhibition (17 ± 0.01 mm), followed by Zr + Ce (15 ± 0.02 mm), Cu + Ce (13 ± 0.02 mm), and Ni + Ce (12 ± 0.01 mm). The standard streptomycin exhibited 23 ± 0.01 mm, while the control showed no inhibition in Fig.-13. The superior antibacterial efficacy of Fe- and Zr-doped films can be attributed to the enhanced generation of reactive oxygen species (ROS) and favourable surface defect states induced by dopant engineering, which disrupt bacterial cell membranes. This nanostructured coating, by eliminating those crucial pathogens, gives you a sturdy approach for biomedical surfaces, and it kind of directly supports the global health

blueprints in Sustainable Development Goal 3 (SDG-3: Good Health and Well-being), so it can help curb the spread of infectious disease transmission.

Table-2: Antibacterial Activity against *Escherichia coli, Pseudomonas aeruginosa, Bacillus subtilis* and *Staphylococcus aureus* measured by Zone of Inhibition (mm)

Sample ID	Zone of Inhibition			
	Escherichia coli	*Pseudomonas aeruginosa*	*Bacillus subtilis*	*Staphylococcus aureus*
Zr+Ce	14±0.02	23±0.01	Nil	15 ± 0.02
Fe+Ce	17±0.01	16±0.02	Nil	17 ± 0.01
Ni+Ce	Nil	13 ±0.01	Nil	12 ±0.01
Cu+Ce	09±0.02	17±0.03	Nil	13 ± 0.02
Std. Streptomycin	26±0.01	25±0.02	19 ±0.01	23 ± 0.01
Control (DMSO)	00	00	00	00

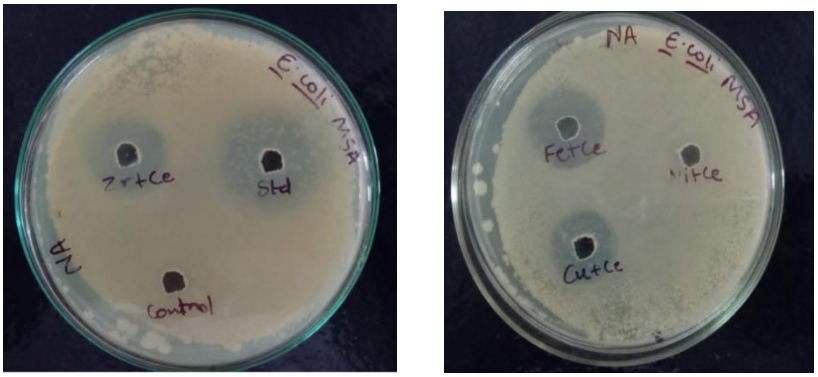

Fig.-10: *Escherichia coli* Inhibition Zone against Doped Zr, Fe, Ni and Cu with Ceria

Figure-10 shows the antibacterial activity of doped ceria nanoparticles against *Escherichia coli*. Zones of inhibition were measured in mm. Fe + Ce showed the highest inhibition among test samples (17 ± 0.01 mm), while Ni + Ce showed no activity. Streptomycin served as the positive control (26 ± 0.01 mm), and DMSO as the negative control.

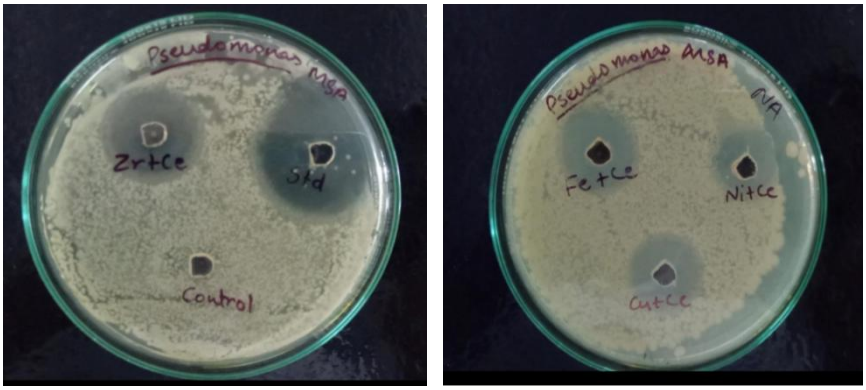

Fig.-11: Pseudomonas aeruginosa Inhibition Zone against Doped Zr, Fe, Ni and Cu with Ceria

Figure-11 Shows the antibacterial effects of doped ceria samples against Pseudomonas aeruginosa. Zr + Ce exhibited the highest activity (23 ± 0.01 mm), followed by Cu + Ce and Fe + Ce. Streptomycin produced a strong inhibition zone (25 ± 0.02 mm), while DMSO showed no effect.

Figure-12 this figure represents the antibacterial response of doped ceria nanoparticles against *Bacillus subtilis*. None of the doped ceria combinations demonstrated inhibitory activity. Only the standard antibiotic Streptomycin showed activity (19 ± 0.01 mm).

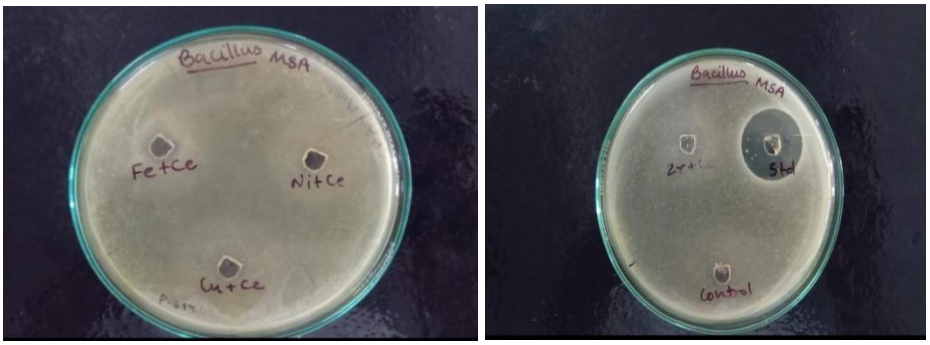

Fig.-12: *Bacillus subtilis* Inhibition Zone against Doped Zr, Fe, Ni and Cu with Ceria



Fig.-13: *Staphylococcus aureus* Inhibition Zone against Doped Zr, Fe, Ni and Cu with Ceria

Figure-13 the Figure displays the zone of inhibition for doped ceria samples tested against *Staphylococcus aureus*. Fe + Ce showed the highest inhibition among the nanoparticle formulations (17 ± 0.01 mm), followed by Zr + Ce, Cu + Ce, and Ni + Ce. Streptomycin again served as the positive control (23 ± 0.01 mm), while DMSO served as the negative control.

The zone of inhibition (in mm) was measured using the agar well diffusion method, with a fixed concentration of 10 mg/ml and a sample volume of 50 µl per well. Streptomycin served as the positive control and DMSO as the negative control. Error bars show the standard error of the mean (SEM) based on triplicate measurements.

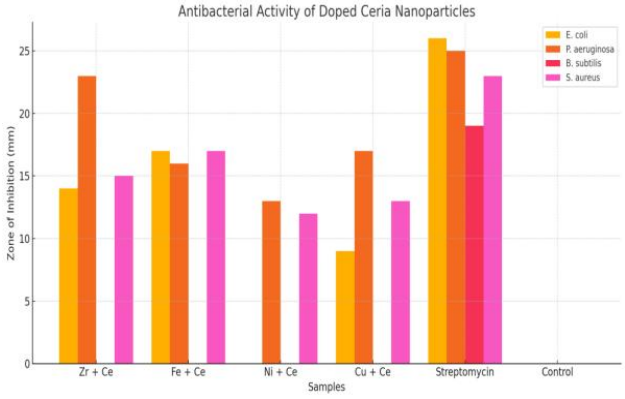

Fig.-14: The overall Graph Illustrates the Antibacterial Activity of Doped Ceria Nanoparticles (Zr + Ce, Fe + Ce, Ni + Ce, Cu + Ce) against Four Bacterial Strains: *Escherichia coli, Pseudomonas aeruginosa, Bacillus Subtilis, and Staphylococcus aureus*

The graph brings out the differential antibacterial response, where Fe/Ce and Zr/Ce had the most significant activity in a way that depends on the strain. Figure-14 also points to that differential antibacterial response, and overall the findings suggest selective, plus strain- dependent antibacterial activity from the doped ceria nanoparticles, with Fe/Ce and Zr /Ce having clear efficacy against multiple strains.

CONCLUSION

In this work, the ultra-spray pyrolysis method was successfully used to create doped ceria (CeO_2) thin films containing Fe, Ni, Cu, and Zr. The structural analysis verified that a cubic fluorite CeO_2 phase was formed, with doping-induced changes in peak broadening and crystallite size. Zr had the highest crystallinity and the least amount of structural distortion among the dopants, whereas Ni-doped films had the highest lattice strain and the smallest crystallite size, indicating a higher concentration of defects. FE-SEM morphological analysis showed that all the doped films have nanoscale, porous and evenly distributed grains with negligible agglomeration, demonstrating the ability of the USP method in preparing high-quality nanostructured coatings. The EDX analysis also confirmed the successful doping of the dopant elements without any impurities, confirming the synthesis process. The antimicrobial assessment showed that Fe- and Zr-doped CeO_2 films exhibited higher antibacterial activity, especially against *Escherichia coli*, *Pseudomonas aeruginosa* and *Staphylococcus aureus*, and Ni-doped films showed comparatively less activity. These results indicate the possibility of dopant engineering to improve the antimicrobial activity of CeO_2 nanomaterials. This work is important for achieving the goals of SDG-3 by providing effective solutions for biomedical and anti-infective coatings, because of the prominent antibacterial performance of Fe- and Zr-doped films. The overall study shows that ultra-spray pyrolysis is a promising technique for the preparation of doped ceria thin films with tunable structural and biological properties for antimicrobial coatings, biomedical devices, and environmental applications. Future work could consider in vivo biocompatibility, long-term stability, and mechanistic studies to better understand the dopant-induced antimicrobial mechanisms.

ACKNOWLEDGMENTS

The author would like to thank the Principal, Yashwantrao Mohite College of Arts, Science and Commerce, Bharathi Vidyapeeth (Deemed to be University), Pune, India, for providing the necessary facilities and support to carry out this work.

CONFLICT OF INTERESTS

The authors declare that there is no conflict of interest.

AUTHOR CONTRIBUTIONS

The present work is related to *SDG-3: Good Health and Well-Being*. All the authors contributed significantly to this manuscript, participated in reviewing/editing and approved the final draft for publication. The research profile of the authors can be verified from their ORCID ids, given below:

Suraj S. Salunkhe http://orchid.org/0009-0000-9012-4151
Sharda R. Gadale http://orchid.org/0000-0002-2872-505X
Supriya S. Shukla http://orchid.org/0000-0002-1581-8599
Avinash B. Pawar http://orchid.org/0000-0003-3420-0476

Open Access: This article is distributed under the terms of the Creative Commons Attribution 4.0 International License (http://creativecommons.org/licenses/by/4.0/), which permits unrestricted use, distribution, and reproduction in any medium, provided you give appropriate credit to the original author(s) and the source, provide a link to the Creative Commons license, and indicate if changes were made.
Cite this article as: S. S. Salunkhe *et al.*, *Rasayan J. Chem.*, 19(4), 2438-2449(2026), https://doi.org/10.31788/RJC.2026.1949786

REFERENCES

1. M. Melchionna, P. Fornasiero and A. Trovarelli, Elsevier, pp. 13-43(2019), https://doi.org/10.1016/b978-0-12-815661-2.00002-5
2. C. Wang, R. Jiang, J. Yang and P. Wang, *Frontiers in Chemistry*, **10**, 892424, https://doi.org/10.3389/fchem.2022.892424
3. T. Vinodkumar, B. G. Rao and B. M. Reddy, *Catalysis Today*, **253**, 57(2015), https://doi.org/10.1016/j.cattod.2015.01.044
4. M. Mohajeri, R. Momenai, S. Karami-Mohajeri, M. Ohadi and M. A. R. Estabragh, *Results in Chemistry*, **15**, 102302(2025), https://doi.org/10.1016/j.rechem.2025.102302

5. P. Sudarsanam, B. Hillary, M. H. Amin, N. Rockstroh, U. Bentrup, A. Brückner and S. K. Bhargava, *Langmuir*, **34(8)**, 2663(2018)
6. H. Mersian, M. Alizadeh and N. Hadi, *Ceramics International*, **44(16)**, 20399(2018), https://doi.org/10.1016/j.ceramint.2018.08.033
7. A. B. Workie, H. S. Ningsih and S. J. Shih, *Journal of Analytical and Applied Pyrolysis*, **170**, 105915(2023), https://doi.org/10.1016/j.jaap.2023.105915
8. S. R. Ardekani, A. S. R. Aghdam, M. Nazari, A. Bayat, E. Yazdani and E. Saievar-Iranizad, *Journal of Analytical and Applied Pyrolysis*, **141**, 104631(2019), https://doi:10.1016/j.jaap.2019.104631
9. J. Leng, Z. Wang, J. Wang, H. H. Wu, G. Yan, X. Li, H. Guo, Y. Liu, Q. Zhang and Z. Guo, *Chemical Society Reviews*, **48(11)**, 3015(2019), https://doi.org/10.1039/c8cs00904j
10. Jin Ho Bang, Yuri T. Didenko, Richard J. Helmich, Kenneth S. Suslick, Material Matters (Sigma-Aldrich), 7(2),2012
11. R. Suresh, V. Ponnuswamy and R. Mariappan, *Applied Surface Science*, **273**, 457(2013), https://doi:10.1016/j.apsusc.2013.02.062
12. P. Wang, F. Meng, C. Gao, W. Xie and A. Li, *Journal of Materials Science: Materials in Electronics*, **29(13)**, 11482(2018), https://doi.org/10.1007/s10854-018-9243-5
13. Xuyang Zhou, Xiao-xiang Yu, Tyler Kaub, Richard L. Martens & Gregory B. Thompson, *Scientific Reports*, **6(1)**, 34642(2016), https://doi.org/10.1038/srep34642
14. V. Pathak, P. Lad, A. B. Thakkar, P. Thakor, M. P. Deshpande and S. Pandya, *Results in Surfaces and Interfaces*, **11**, 100111(2023), https://doi.org/10.1016/j.rsurfi.2023.100111
15. I. Boudene, M. Oubakalla, Y. Nejmi, M. Beraich, H. Majdoubi, R. A. Belakhmima, R. Bouhfid and M. Ebn Touhami, *Journal of Energy Storage*, **117**, 116248(2025), https://doi.org/10.1016/j.est.2025.116248
16. R. S. Prakash, C. Mahendran, J. Chandrasekaran, R. Marnadu and S. Maruthamuthu, *Applied Physics A*, **127(3)**, 173(2021)
17. X. Cao, S. Zhao, S. Yan, J. Hu and Y. Dan, *Journal of Renewable Materials*, **8(11)**, 1443(2020), https://doi.org/10.32604/jrm.2020.012113
18. L. S. R. Rocha, R. A. C. Amoresi, H. Moreno, M. A. Ramirez, M. A. Ponce, C. R. Foschini, E. Longo and A. Z. Simões, *ACS Omega*, **5(25)**, 14879(2020), https://doi.org/10.1021/ACSOMEGA.9B04250
19. I. S. Hussen and J. M. Rzaij, *Passer Journal of Basic and Applied Sciences*, **8(1)**, 148(2026), 10.24271/psr.2025.516655.2074
20. J. Zimou, K. Nouneh, R. Hsissou, A. El-Habib, L. El Gana, A. Talbi, M. Beraich, N. Lotfi and M. Addou, *Materials Science in Semiconductor Processing*, **135**, 106049(2021), https://doi.org/10.1016/J.MSSP.2021.106049
21. L. Tang, Z. Pan, J. Zhao and J. Zhai, *Chemical Engineering Journal*, **455**, 140524(2023), https://doi.org/10.1016/j.cej.2022.140524
22. R. Munirathnam, S. M. Rumana Farheen, S. Manjunatha, H. C. Manjunatha, Y. S. Vidya and S. Krishnaveni, *Journal of Science: Advanced Materials and Devices*, **8(17)**, 100551(2023), https://doi.org/10.1016/j.jsamd.2023.100551
23. K. J. Kim, Y. J. Kim, D. H. Kim, G. R. Hong, Y. L. Lee, K. Lee and H. S. Roh, *Chemical Engineering Journal*, **495**, 153634(2024).
24. N. T. Luong, H. Okumura, E. Yamasue and K. N. Ishihara, *Royal Society Open Science*, **6(2)**, 181861(2019).
25. S. Shanmugasamy, K. Balakrishnan, A. Subasri, S. Ramalingam and A. Subramania, *Journal of Rare Earths*, **36(12)**, 1319(2018), https://doi.org/10.1016/j.jre.2018.06.004
26. V. I. Popkov, V. P. Tolstoy and V. N. Nevedomskiy, *Heliyon*, **5(3)**, e01443(2019), https://doi.org/10.1016/j.heliyon.2019.e01443
27. O. L. Pop, A. Mesaroș, D. C. Vodnar, R. Suharoschi, F. Tăbăran, L. Mageruşan, I. S. Tódor, Z. Diaconeasa, A. Balint, L. Ciontea and C. Socaciu, *Nanomaterials*, **10(8)**, 1614(2020), https://doi.org/10.3390/nano10081614
28. M. A. Dar, R. Gul, P. Karuppiah, N. A. Al-Dhabi and A. A. Alfadda, *Crystals*, **12(2)**, 179(2022), https://doi.org/10.3390/cryst12020179

[RJC-9786/2026]